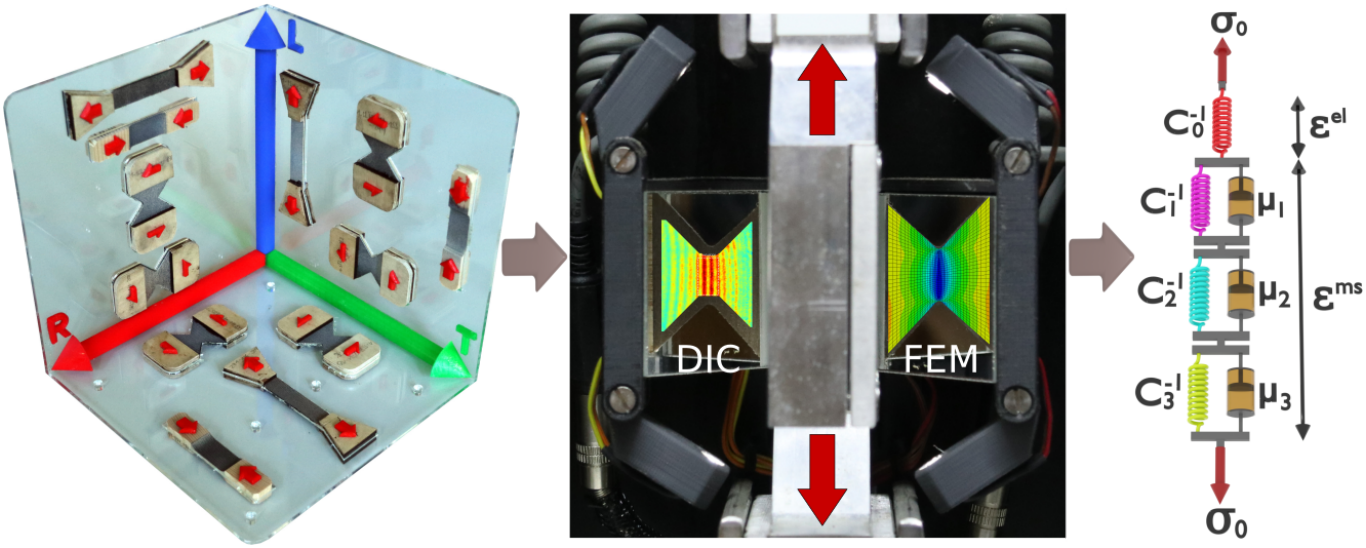
Graphical Abstract

Orthotropy of wood mechanosorption in Norway spruce

Jonas M. Maas, Falk K. Wittel



Highlights

Orthotropy of wood mechanosorption in Norway spruce

Jonas M. Maas, Falk K. Wittel

- Quantitative measurement and comparison of mechanosorptive creep orthotropy
- Rheological model based on experimental data in all anatomical directions
- Tests must account for nonuniform stress and moisture field evolution
- Mechanosorption is only groupwise scalable from elasticity and viscoelasticity
- Models must capture significant mechanosorptive compression-tension asymmetry

Orthotropy of wood mechanosorption in Norway spruce

Jonas M. Maas[a], Falk K. Wittel[a]

[a] *ETH Zürich, Institute for Building Materials, Laura-Hezner-Weg 7, 8093 Zurich, Switzerland*

Abstract

Mechanosorption refers to the increase in creep deformation under load and simultaneous moisture changes. It is the dominant deformation mechanism in wood, yet the least understood. Due to difficulties in isolating it from the total deformation, there is a lack of consistent experimental data regarding anisotropy and species. This led to oversimplified rheological models of wood. To overcome this, the present study assesses a full set of orthotropic mechanosorptive parameters for a single Norway spruce stem. To account for nonuniform stress and moisture fields, a coupled experimental-numerical approach is implemented. It considers moisture-dependent elasticity, plasticity, viscoelasticity, and hygroexpansion, obtained in a previous work for the same tree. The present study identifies the most relevant orthotropic differences, including compression-tension and shear asymmetries. Similarities in directional behavior are clustered into non-trivial scaling groups with respect to elastic and viscoelastic behavior. The findings of this study are integrated into a popular rheological model for Norway spruce, implemented as a publicly available Abaqus User Material. The obtained data have a degree of completeness to serve as a reference dataset for future rheological models of wood.

Keywords:
hygro-elasticity, mechanosorption, strain decomposition, compression-tension asymmetry, shear asymmetry, Abaqus UMAT

1. Introduction

Over their service lives, seasonal climatic changes alter stress and strain states in timber structures, causing deformations that deviate from the initial design. The development of complex wooden structures is therefore often accompanied by hygromechanical Finite Element (FE) models of wood. Under changing relative humidity (RH), one of the most relevant mechanisms to consider is mechanosorption (MS), which accumulates deformations that strongly exceed elastic ones (Armstrong and Christensen, 1961; Bengtsson, 1999; Toratti and Svensson, 2000; Entwistle and Zadoroshnyj, 2008; Ferrara and Wittel, 2026a). Adequate predictions of MS within constitutive models for FE simulations thus require a comprehensive quantification of orthotropic MS parameters.

MS creep is induced by changes in moisture content (MC) under mechanical load (Armstrong and Christensen, 1961). The strain response is driven by the magnitude of moisture change (Gibson, 1965; Schniewind, 1966; Grossman, 1976; Hunt, 1999) and is particularly large during the first adsorption and desorption cycle after load application (Ranta-Maunus, 1975; Grossman, 1976; Entwistle and Zadoroshnyj, 2008). In subsequent moisture cycles, the deformation increments gradually decrease (Grossman, 1976; Hunt, 1999; Armstrong and Christensen, 1961; Ranta-Maunus, 1975). Upon removal of load, MS-strains remain frozen until additional moisture cycles release them (Ranta-Maunus, 1975; Grossman, 1976; Entwistle and Zadoroshnyj, 2008). Armstrong and Christensen (1961) claimed that an irrecoverable portion remains but neglected scleronomic plastic strain.

Many scientists (e.g., Gibson, 1965; Kauman, 1966; Schniewind, 1966; Grossman, 1976; Gril, 1987) link these observations to the continuous reformation of hydrogen bonds between the cellulose chains and hemicellulose during water sorption. The breaking of hydrogen bonds leaves an unsaturated hydroxyl group in an unstable state, driving molecular rearrangements. Under mechanical load, these rearrangements can cause relative slip between microfibrillar aggregates, increasing deformation. These slips are locked by the reformed hydrogen-bond network and are unlikely to reverse upon load removal, resulting in residual stress. Consecutive moisture changes remobilize the hydrogen-bond network, allowing recovery of frozen MS strains by reverse slips. This slip-stick idea is supported by simulations, e.g., those of Navi et al. (2002) and Amando de Barros and Wittel (2026). The latter developed a stick-slip fiber bundle model (SS-FBM) in which slips occur due to changes in MC. It reproduces wood's full hygromechanical behavior within a unified framework. Further support comes from infrared spectroscopy measurements by Olsson and Salmén (2001) and Stevanic and Salmén (2020),

Email addresses: jomaas@ethz.ch (Jonas M. Maas), fwittel@ethz.ch (Falk K. Wittel)

which experimentally confirmed the fiber slippage and the rearrangement of water molecules within hydrogen bonds during MS creep.

While the SS-FBM respects the microstructural mechanism of MS well, it is purely one-dimensional and not applicable to multi-axial states. Therefore, constitutive models are utilized that are implemented for FE frameworks. They commonly use Kelvin-Voigt (KV) series in the moisture-change domain, with or without friction elements (e.g., Leicester, 1971; Svensson and Toratti, 2002; Hanhijärvi and Mackenzie-Helnwein, 2003; Fortino et al., 2009; Hassani et al., 2015; Yu et al., 2022). However, they require well-defined material parameters that preserve wood's orthotropic nature.

Experimentally determined MS model parameters must respect intrinsic material symmetries (Grossman, 1976; Peng et al., 2019, 2020). They are nonproportional to elastic compliance (Ferrara and Wittel, 2026a), vary with loading type (Grossman, 1976), and increase with applied stress. In particular, creep under compression is significantly larger than under tension (Bengtsson, 1999; Toratti and Svensson, 2000). For low loading degrees (LD, stress w.r.t. strength), the MS strains are proportional to the applied stress, with stress-independent creep compliances (Liu, 1993; Wu and Milota, 2007; Olsson et al., 2007). At higher LDs, the creep compliance becomes stress-dependent (Hunt, 1989; Liu, 1993; Ferrara and Wittel, 2026a). Estimates for the transition are around 30 % LD, following Liu (1993) and Zhou et al. (2000). In addition, MS creep varies with MC, showing very low magnitudes below 65 % RH (Liu, 1993). It is independent of whether MS started in the dry or moist state (Bengtsson, 2001). Note that in a deformed state, the equilibrium MC depends on the volumetric strain, causing increased sorptivity under dilation and decreased sorptivity under contraction of the pore space (Barkas, 1949; Skaar, 1988). This behavior was shown by Olsson and Salmén (2001), where the MC in paper fibers at 90 % RH increases in tensile creep over time.

The influence of MS parameters shows that a holistic orthotropic description of MS requires compression, tension, and shear tests in all main anatomical directions, across multiple LDs, and under different moisture histories. In reality, experimental tests are limited to specific stress states. Bending tests with grain direction being coaxial to the neutral axis are a simple setup, conducted on various species such as blue gum and Klinki pine (Armstrong and Christensen, 1961), Scots pine (Toratti, 1992; Mohager and Toratti, 1992; Hanhijärvi and Hunt, 1998), Norway spruce (Toratti, 1992; Bengtsson, 2001), European beech (Hering, 2011), or various Japanese species (Zhou et al., 1999, 2000). Although the test seems simple to perform, a clean evaluation is nearly impossible given wood's highly nonlinear hygro-mechanical behavior described above. Uni-axial compression tests were performed for various combinations of anatomical directions and species, such as the tangential (T) direction for Scots pine (Svensson and Toratti, 2002), small-leaved lime (Stöcklein et al., 2024), or European oak (Huč et al., 2018), or for spruce in the longitudinal (L) direction (Bažant and Meiri, 1985; Bengtsson, 1999) or perpendicular to it (Massaro and Malo, 2019). For tension, tests were conducted in the three main anatomical directions for Chinese fir (Peng et al., 2019, 2020), in the radial (R) direction for Norway spruce (Froidevaux et al., 2012; Ferrara and Wittel, 2026a), in the L direction for Maritime pine (Navi et al., 2002), Norway spruce (Bengtsson, 1999), or Silver fir (Saifouni et al., 2016), and in the T direction for European beech (Schniewind, 1966), Scots pine (Svensson and Toratti, 2002), Douglas fir (Wu and Milota, 2007), or Norway spruce (Ferrara and Wittel, 2026a). Further studies include torsion tests around the L axis for Monterey pine (Entwistle and Zadoroshnyj, 2008) and single-fiber tests (Olsson and Salmén, 2001; Olsson et al., 2007).

All these studies are limited to specific species and stress states, exhibiting a lack of a comprehensive orthotropic investigation for at least one species. This data gap strongly affects the accuracy of moisture-dependent hygromechanical simulations of wood. Consequently, popular models for Norway spruce and beech (Fortino et al., 2009; Hassani et al., 2015; Yu et al., 2022) account only for relative creep in the T and L directions. Parameters were partly borrowed from similar species, and missing components were proportionally scaled with the elastic compliance. This inevitably leads to inaccuracies in creep predictions perpendicular to the grain or under shear, where scaling is not based on experimental insights.

This paper aims to close the data gaps for Norway spruce, one of Europe's most common construction woods, by conducting MS compression, tension, and shear experiments in all main anatomical directions. By determining the full orthotropy of the MS compliance matrix, one can make recommendations for the scope of future studies and parameter scaling procedures. Ultimately, this yields more robust assumptions for hygro-mechanical simulations in environments with changing climatic conditions.

2. Methods

This study presents the results of mechanosorptive tests on Norway spruce in three compression and three tension, as well as six shear directions (12 in total). Sec. 2.1 describes the test setups that capture total strain evolution under repeated moisture cycles. Since the total strain also includes elastic, viscoelastic, and hygroresponsive components, it must be decomposed to isolate the MS strain. This is achieved by simulating digital twins of the experiments using a hygromechanical FE model as a basis for fitting the MS parameters. Sec. 2.2 describes the parameter identification for calculating the moisture evolution, while Sec. 2.3 details the strain decomposition and the corresponding parameter fitting.

2.1. Mechanosorptive tests

To investigate the 12 stress states within a reasonable time frame at identical climate history, the experiments (see Fig. 1) were parallelized using a 12-axis computer-controlled, climatized creep rack. Sample shapes, experimental setup, and data processing are described in detail in Maas and Wittel (2025). To summarize, the used geometries have a dogbone shape for compression and tension tests and an Arcan shape for shear tests. All geometries have a cross-section thickness of 4 mm to achieve short equilibration times. The samples were equilibrated at 65 % RH and 20 °C for manufacturing, storage, and mounting into the sample holders. They always contained at least four annual rings to approximate material homogeneity.

All tests comprise a constant applied load and repeated moisture cycles from 35 % to 90 % RH at 21.9 ± 0.5 °C, which corresponds to 8.0 ± 0.1 % and 19.5 ± 0.1 % MC, as verified on twin samples. The sample catalog (see Tab. 1) gives the number of samples per loading case and the applied LDs. As the LD η_{RH} gives the ratio of actual stress to average moisture-dependent strength, we use values reported by Maas and Wittel (2026a), obtained from samples extracted from the same tree. Note that LDs for R and T compressive states are quite low, as samples already fail at $\eta_{90\%} \approx 0.3$ when exposed to cyclic moisture. At the start of each test, samples are mounted in the creep rack at 65 % RH and consecutively equilibrated to 35 % RH, before load application. After loading, the samples undergo 6 full 36 h moisture cycles, holding each RH level for 18 h. Tests on twin samples showed that after 18 h, the MC change is less than 0.04 %/h. At the end of the sixth cycle, the load is removed, and four additional cycles are conducted to capture MS strain recovery. In total, one realization runs for 15 days. Throughout the experiment, the climate is tracked

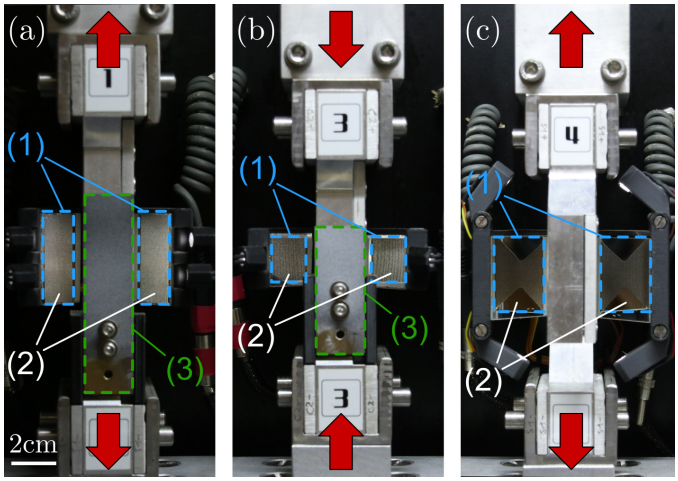


Figure 1: Creep experiment setup for (a) compression, (b) tension, and (c) shear loading. Red arrows denote the load application. A camera records the sample surfaces (1) through mirrors (2), and (3) are brass reference samples for measuring changes in the DIC system's optical path caused by possible temperature changes of the creep rack during long-lasting test runs.

Table 1: Tested MS samples with their recorded axial and lateral anatomical direction. n denotes the number of samples, σ the applied stress, and $\eta_{35\%}$ and $\eta_{90\%}$ the LD relative to their strength at 35 % and 90 % RH (Maas and Wittel, 2026a).

Axial	Lateral	n	σ [MPa]	$\eta_{35\%}$ [−]	$\eta_{90\%}$ [−]
Compression					
L	T	10	−9.51	0.18	0.31
R	L	8	−0.64	0.13	0.18
T	R	9	−0.58	0.08	0.13
Tension					
L	T	9	38.94	0.28	0.32
R	L	8	1.22	0.18	0.26
T	R	6	1.19	0.24	0.32
Shear					
L	R	8	1.39	0.21	0.30
L	T	6	1.33	0.18	0.26
R	L	7	1.92	0.21	0.29
R	T	6	0.56	0.24	0.32
T	L	8	1.75	0.20	0.27
T	R	6	0.55	0.40	0.43

with a B+B HYTE-ANA-1735 moisture sensor with an accuracy of 3 % RH. Surface strain fields are sampled hourly using digital image correlation (DIC) with MATLAB Ncorr (Blaber et al., 2015) and reduced to a scalar strain value by applying the evaluation protocol described in Maas and Wittel (2025). To account for out-of-plane displacements induced by hygroexpansion, the systematic relationship between displacement and 2D DIC error was quantified and used to correct the measured strains.

2.2. Identification of moisture transport parameters

Determining MS parameters from creep tests requires detailed knowledge of the moisture field within samples. Typically, moisture is calculated via moisture transport FE simulations with trustworthy model parameters. Within this study's climatic window, the MC is always below fiber saturation, and transport is governed by diffusion and surface moisture transfer. Consequently, one requires diffusion coefficients in different anatomical directions, their respective moisture dependencies, and a surface-film coefficient. In this work, the diffusive transport parameters are inversely determined by minimizing the discrepancy between the average MC evolution from moisture-transport FE simulations and corresponding sorption tests in climate chambers. The utilized samples were of identical thickness as the creep samples and equilibrated in the creep rack's climate chamber from 90 % to 35 % RH and in another climate chamber from 35 % to 95 % RH. Their mass m_ω was tracked with a Mettler Toledo AE 200 weight scale with 0.1 mg accuracy once directly before the test, every 1 h during the first 12 h, and every 12 h within the subsequent 36 h of equilibration. After oven-drying at 103 °C, the MC $\omega = (m_\omega - m_0)/m_0$ could be calculated using the oven-dry mass m_0. During adsorption, a Voltcraft DL-121TH

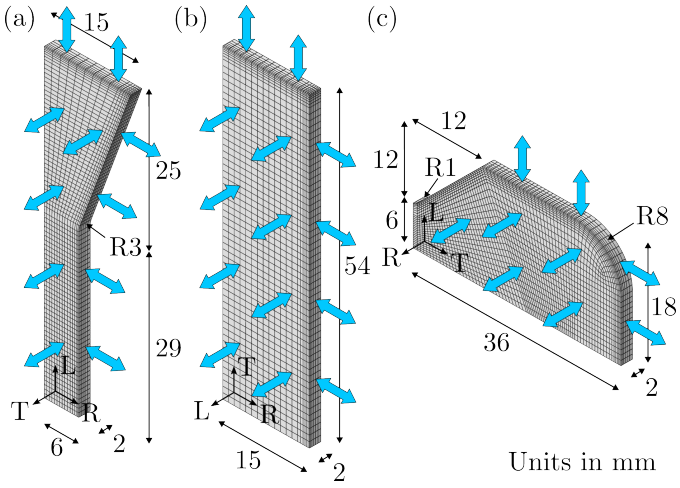


Figure 2: FE model for fitting moisture diffusion for the three sample types where the thickness matches the (a) T, (b) L, and (c) R direction. Each mesh resembles 1/8 of a sample, with symmetry along the RT, RL, and TL planes. The blue arrows denote the moisture exchange with the environment.

multi-datalogger tracked the environmental RH with ±3 % accuracy. A total of six samples were tested per transport direction, consistent with the sample thickness.

The obtained mass evolution is compared with results from the FE model (see Fig. 2), which implements a simple orthotropic Fickian diffusion model. The parameters for the transport model are estimated using an inverse approach with the MATLAB Surrogate Model Toolbox (MATSuMoTo) (Müller, 2014). In detail, the FE model uses the analogy between Fick's and Fourier's laws, assuming unit density and specific heat. The mesh consists of quadratic heat-transfer elements (DC3D20) with element size ranging from 0.5 mm (Figs. 2a and b) and 0.7 mm (Fig. 2c) in the samples' center to 0.2 mm towards the samples' outer boundaries. The initial uniform moisture field corresponds to the experimental MC measured before each sorption test. A surface film condition with a constant film coefficient controls the moisture flux from the environment into the sample. The boundary MCs are applied on the samples' outer surfaces (see blue arrows in Fig. 2) through an embedded film coefficient h_M (Siau and Avramidis, 1996), as

$$J_s = h_M(\omega_\mathrm{s} - \omega_\mathrm{eq,sink}). \tag{1}$$

J_s is the MC flux from the wood surface to the environment, ω_s is the MC at the sample surface, and $\omega_\mathrm{eq,sink}$ is the material's equilibrium MC with the environment's RH. It is derived from the sorption isotherm of Maas and Wittel (2026a) and linearly scaled at the known upper and lower RH (35 %, 90 % RH) to correct for the small difference between the sample and the average sorption behavior of the tree.

The moisture diffusion inside the sample is moisture-dependent and simplifies for a uniform density to (Siau, 1984; Hassani et al., 2015)

$$\frac{\partial \omega}{\partial t} = \nabla \cdot (\boldsymbol{D}(\omega)\nabla\omega)\,. \tag{2}$$

Here, $\boldsymbol{D}(\omega) = \mathrm{diag}\,(D_R(\omega), D_T(\omega), D_L(\omega))$ contains the directional diffusivity. The diffusion coefficients $D_i(\omega)$ in anatomical direction $i \in \{R, T, L\}$ are (Toratti, 1992; Hassani et al., 2015)

$$D_i(\omega) = D_{0,i}\exp(\alpha_i\omega) \quad \text{for} \quad \omega \le \omega_\mathrm{FS}. \tag{3}$$

$D_{0,i}$ denotes the diffusion coefficient at 0 % MC, α_i is an exponential scaling coefficient, ω is the MC, and $\omega_\mathrm{FS} = 0.28$ (Maas and Wittel, 2026a) is the MC at fiber saturation.

$D_{0,i}$, α_i, and h_M are the fitting coefficients of the transport model. Since the simulations are computationally expensive, this study uses surrogate modeling to determine $\boldsymbol{D}(\omega)$ with a least-squares fit that minimizes the difference between experimental and simulated total MC. The surrogate model uses a cubic radial basis function (RBFcub), a Latin hypercube design (LHS), and randomized sampling (CANDglob) with 128 iterations to solve the initial minimization problem. A local minimum prediction (SurfMin), with an additional 128 iterations, subsequently refines this initial solution to find the final optimum.

2.3. Decomposition of strains

The moisture field within the samples has gradients that induce restrained stresses due to hygroexpansion. Hence, the measured total strains ($\boldsymbol{\epsilon}^\mathrm{tot}$) of the MS tests superpose elastic ($\boldsymbol{\epsilon}^\mathrm{el}$), possibly plastic ($\boldsymbol{\epsilon}^\mathrm{pl}$), hygroexpansive ($\boldsymbol{\epsilon}^\omega$), viscoelastic ($\boldsymbol{\epsilon}^\mathrm{ve}$), and MS strains ($\boldsymbol{\epsilon}^\mathrm{ms}$) as

$$\boldsymbol{\epsilon}^\mathrm{tot} = \boldsymbol{\epsilon}^\mathrm{el} + \boldsymbol{\epsilon}^\mathrm{pl} + \boldsymbol{\epsilon}^\omega + \boldsymbol{\epsilon}^\mathrm{ve} + \boldsymbol{\epsilon}^\mathrm{ms}. \tag{4}$$

A clean assessment of the MS parameters thus requires isolating $\boldsymbol{\epsilon}^\mathrm{ms}$ by decomposing $\boldsymbol{\epsilon}^\mathrm{tot}$ into its respective strain components while accounting for moisture and stress fields. The present study achieves this decomposition by simulating digital twins of the experiments in a three-dimensional FE model with Abaqus (Dassault Systèmes, 2021). It uses the rheological model of Hassani et al. (2015), implemented as a User Material (UMAT), to calculate the orthotropic and moisture-dependent strain components in Eq. 4. To achieve high accuracy, the UMAT's calculation of $\boldsymbol{\epsilon}^\mathrm{el}$, $\boldsymbol{\epsilon}^\mathrm{pl}$, $\boldsymbol{\epsilon}^\omega$, and $\boldsymbol{\epsilon}^\mathrm{ve}$ was updated with the material parameters from Maas and Wittel (2026a), who quantified the moisture-dependent elasticity, plasticity, hygroexpansion, and viscoelasticity in all main anatomical directions, including shear. These material parameters originate from samples manufactured from the same tree as those tested in the present study, ensuring parameter consistency. Sec. Appendix A documents the related updates to the original UMAT and explains how it calculates each strain component, besides $\boldsymbol{\epsilon}^\mathrm{ms}$.

The UMAT calculates $\boldsymbol{\epsilon}^\mathrm{ms} = \sum_{k=1}^{n=3} \boldsymbol{\epsilon}_k^\mathrm{ms}$ through a series of n KV elements, in which the dashpots respond to changes

in MC ω (Fortino et al., 2009; Hassani et al., 2015). The k-th KV element's strain $\boldsymbol{\epsilon}_k^{\mathrm{ms}}$ relates to the applied time-dependent stress $\boldsymbol{\sigma}(t)$ as

$$\dot{\boldsymbol{\epsilon}}_k^{\mathrm{ms}}(t,\omega) = \frac{|\dot{\omega}|}{\mu_k}\left(\boldsymbol{C}_k^{-1}(\omega)\cdot\boldsymbol{\sigma}(t) - \boldsymbol{\epsilon}_k^{\mathrm{ms}}(t,\omega)\right). \tag{5}$$

Here, μ_k is the characteristic moisture change of the k-th KV element, and $\boldsymbol{C}_k^{-1}$ is the corresponding spring compliance. In the original model, the compliance in the L direction originates from bending tests (Toratti, 1992), while a proportionality factor γ_k, which derives from tangential experiments (Svensson and Toratti, 2002), scales the remaining $\boldsymbol{C}_k^{-1} = \boldsymbol{C}_0^{-1}/\gamma_k$ by the elastic compliance $\boldsymbol{C}_0^{-1}$. To avoid such generalized scaling, the present study aims to determine all nine independent orthotropic components of $\boldsymbol{C}_k^{-1}$. Thus, it extends the UMAT to calculate $\boldsymbol{C}_k^{-1} = \boldsymbol{\Gamma}_k \circ \boldsymbol{C}_0^{-1}$ with a fully orthotropic scaling matrix

$$\boldsymbol{\Gamma}_k = \begin{bmatrix} \Gamma_{x,RR}^{(k)} & \Gamma_{x,TR}^{(k)} & \Gamma_{x,RL}^{(k)} & 0 & 0 & 0 \\ & \Gamma_{x,TT}^{(k)} & \Gamma_{x,LT}^{(k)} & 0 & 0 & 0 \\ & & \Gamma_{x,LL}^{(k)} & 0 & 0 & 0 \\ & & & \Gamma_{s,RT}^{(k)} & 0 & 0 \\ & \text{sym.} & & & \Gamma_{s,RL}^{(k)} & 0 \\ & & & & & \Gamma_{s,LT}^{(k)} \end{bmatrix}. \tag{6}$$

$\Gamma_{x,ij}^{(k)}$ corresponds to the strains in direction j from a uniaxial load in direction i, and $\Gamma_{s,ij}^{(k)} = \Gamma_{s,ji}^{(k)}$ corresponds to the shear strains in a shear plane normal to i caused by a load in direction j.

The present study determines an initial guess of $\boldsymbol{\Gamma}_k$ from fitting a one-dimensional serial model of elasticity (Eq. A.1), viscoelasticity (Eq. A.3), and MS (Eq. 5) to the experimental creep strains at the end of each moisture cycle. Here, $\Gamma_{x,RR}$, $\Gamma_{x,TT}$, and $\Gamma_{x,LL}$ derive from the axial strains of the R, T, and L uniaxial tests, and $\Gamma_{x,RL}$, $\Gamma_{x,TR}$, and $\Gamma_{x,LT}$ from their corresponding lateral strains. $\Gamma_{s,ij}$ and $\Gamma_{s,ji}$ result from the shear tests in the corresponding shear planes ij and ji. As this approach does not account for plasticity or stress and moisture gradients within the sample, these parameters are only suitable as an initial guess for subsequent fitting of $\boldsymbol{\Gamma}_k$ with the FE model.

To determine $\boldsymbol{\Gamma}_k$, the applied RH, loads, and strain responses from the experiments in Tab. 1 are averaged at each time step across all samples of the same type, yielding an average time-dependent curve before fitting. Then, these average experiments are simulated using the FE model of the mechanically relevant sample section (see Fig. 3). In the models, the samples' anatomical directions from Tab. 1 align with the depicted Cartesian coordinate system, except for shear samples in the RT and TR planes, which use a radial coordinate system centered at the samples' pith location, which was determined prior to the sample extraction from the stem. First, the moisture fields are calculated with the fitted moisture-transport model (Sec. 2.2).

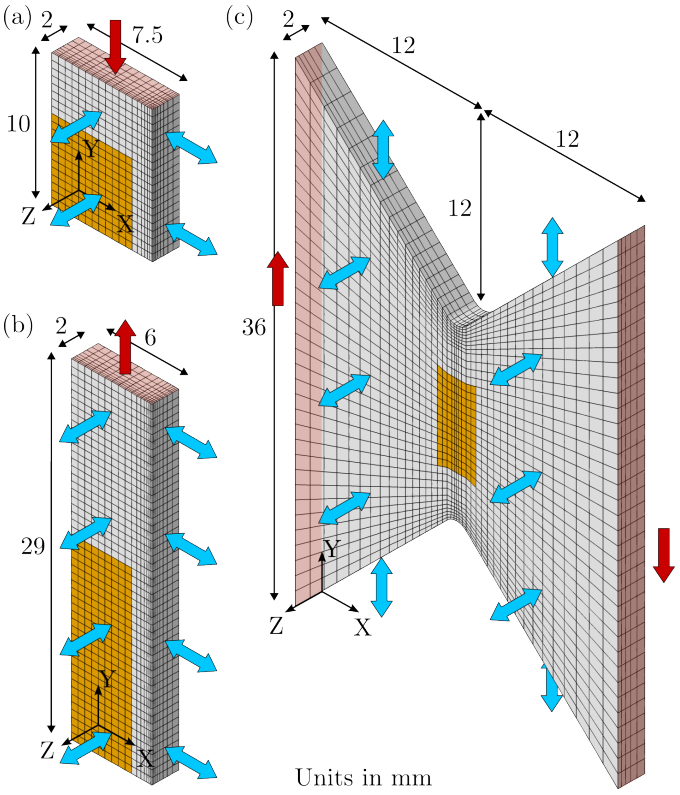


Figure 3: FE model for sequentially coupled moisture-stress analysis. Compression (a) and tension (b) samples have XY, XZ, and YZ symmetry, and shear samples (c) have XY symmetry. Forces (red arrows) act uniformly on red surfaces, which block out-of-plane rotations and enforce equal normal nodal displacements. The shear sample's left red surface constrains X-displacements, and its lower edge constrains Y-displacements. Blue arrows show environmental moisture exchange, and orange elements denote the strain response's averaging region.

These results are used in the coupled mechanical simulation to calculate the strain response using the UMAT with standard 3D stress quadratic elements with reduced integration (C3D20R). Element sizes range from 0.5 mm to 0.1 mm for compression (Fig. 3a) and tension (Fig. 3b) samples, and from 1.5 mm to 0.2 mm for shear (Fig. 3c) samples. The uniaxial models represent 1/8 of the sample with three symmetry planes, and apply the load as equally distributed pressure on the top surface. Boundary conditions prevent out-of-plane rotations of the top plane, whose vertical displacements are constrained to a common reference point. In contrast, the shear models represent 1/2 of the sample with a single symmetry plane because symmetric hygroexpansion combined with antisymmetric loads precludes the use of symmetry or antisymmetry in the XZ and YZ planes. The loads are applied at reference points connected to the left and right boundaries of the notched square via continuum-distributed coupling in all translational directions, without constraining hygroexpansion. A Z-axis rotation constraint at the left and right boundaries prevents sample rotation. To avoid numerical singularity, the X movement of the left boundary and the Y movement of its lower edge are constrained, even though the vertical

reaction force is zero, equal to the sum of external forces in the Y direction. All models' strain responses are reduced to a scalar by averaging the strains over a 0.2 mm- thick layer (highlighted in orange in Fig. 3), matching the surfaces evaluated in the creep experiments.

Because of the high computational cost per iteration, a surrogate model is again used to determine $\mathbf{\Gamma}_k$ by least-squares minimization of the discrepancy between the simulations' strain response and the averaged experimental data. Here $\mathbf{\Gamma}_k$ are determined with respect to the samples' elastic compliance, obtained from the instantaneous deformation upon load application. $\Gamma_{x,RR}$ and $\Gamma_{x,RL}$ are fitted to the R, $\Gamma_{x,TT}$ and $\Gamma_{x,TR}$ to the T, and $\Gamma_{x,LL}$ and $\Gamma_{x,LT}$ to the L uniaxial samples, where $x \in \{c, t\}$ differentiates between compression (c) and tension (t) tests. After updating the UMAT with these parameters, a subsequent fit determines all $\Gamma_{s,ij}$ and $\Gamma_{s,ji}$ from the shear tests. In each fitting, the surrogate model uses an initial Latin hypercube design (LHS), a cubic radial basis function surrogate model (RBFcub), and randomized global sampling (CANDglob) with 64 iterations for uniaxial samples and 35 iterations for shear samples.

3. Results

Valid characterization of MS behavior requires a deep understanding of the moisture and strain fields. Sec. 3.1 presents the sorption curves and parameters of the fitted diffusion model, while Sec. 3.2 provides the total strain responses of the MS experiments, along with the fitted model response. As it is not feasible for most scientific studies to experimentally determine MS parameters in all anatomical directions, data reduction strategies for the fitted MS parameters are required. Hence, Sec. 3.3 evaluates the orthotropy of the isolated MS creep compliance, and presents its scaling relations with elastic and viscoelastic compliances from Maas and Wittel (2026a).

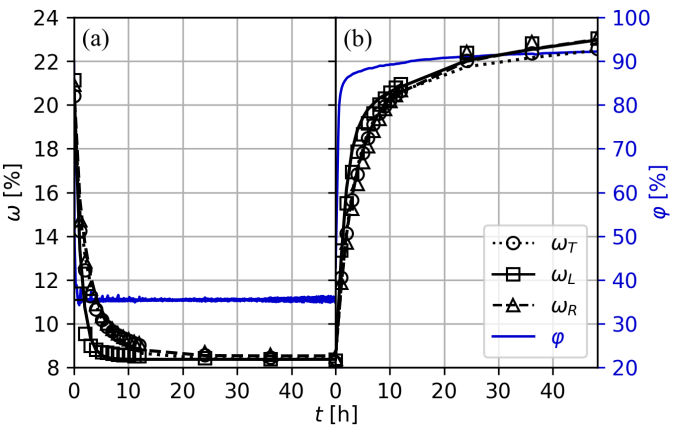


Figure 4: Fitted (lines) and experimental (markers) moisture content ω_i over time t for desorption (a) and adsorption (b). i denotes the main diffusion direction for each sample type (see Fig. 2). φ is the relative humidity of the environment.

3.1. Diffusion coefficients

Accurately describing the creep samples' moisture field is critical for predicting internal stresses. Sorption tests provide total MC evolution, which serves as the basis for inverse parameter identification of the Fickian diffusion model. In Fig. 4, the markers indicate the experimental sorption curves, and the lines show the model response using the model described in Sec. 2.2. ω_i is the total MC for the samples with main diffusion direction i (see Fig. 2), t is the time, and φ is the environment's RH. φ, and thus the applied equilibrium MC at the boundary of the fitted diffusion model, is constant for desorption (Fig. 4a), while it steadily increases for adsorption (Fig. 4b). This increase is attributed to moisture dynamics in the climate chamber used, but it does not affect the measured ω_i at $\varphi = 90\,\%$, which is identical for desorption and adsorption tests.

The parameters of the fitted moisture-dependent diffusion coefficients (Eq. 3) are

$$\begin{aligned} D_{0,R} &= 0.341\,\mathrm{mm^2/h}, \quad \alpha_R = 2.995, \\ D_{0,T} &= 0.304\,\mathrm{mm^2/h}, \quad \alpha_T = 3.574, \\ D_{0,L} &= 1.776\,\mathrm{mm^2/h}, \quad \alpha_L = -1.408. \end{aligned} \tag{7}$$

The corresponding surface emission coefficient (Eq. 1) is $h_M = 10.488\,\mathrm{mm/h\%}$. Due to the sign of α_i, $D_R(\omega)$ and $D_T(\omega)$ increase with increasing MC, while $D_L(\omega)$ decreases. This fitted model is used to calculate the moisture field within the MS creep samples, which serves as input to the subsequent stress analysis.

3.2. Total strain response

The total strain in an MS test comprises multiple rheological mechanisms (see Eq. 4), whose strain responses are highly inhomogeneous throughout the sample due to

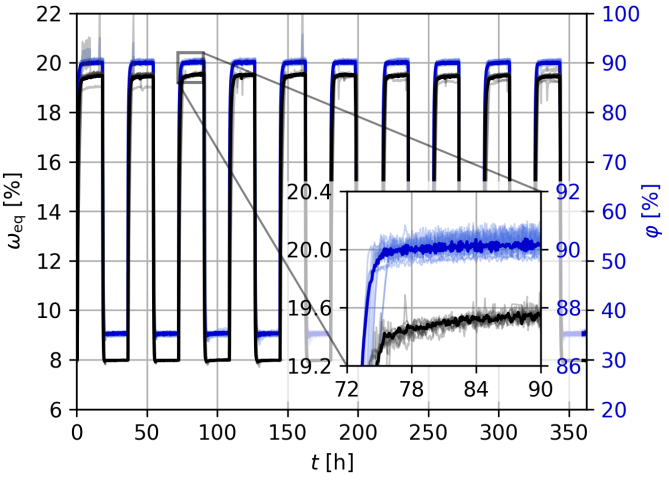


Figure 5: Climate conditions of the creep experiments. The equilibrium moisture content ω_{eq} over time t is calculated from the measured relative humidity φ using a scaled sorption isotherm. Opaque lines represent the average climate evolution over all tests, while translucent lines represent individual tests.

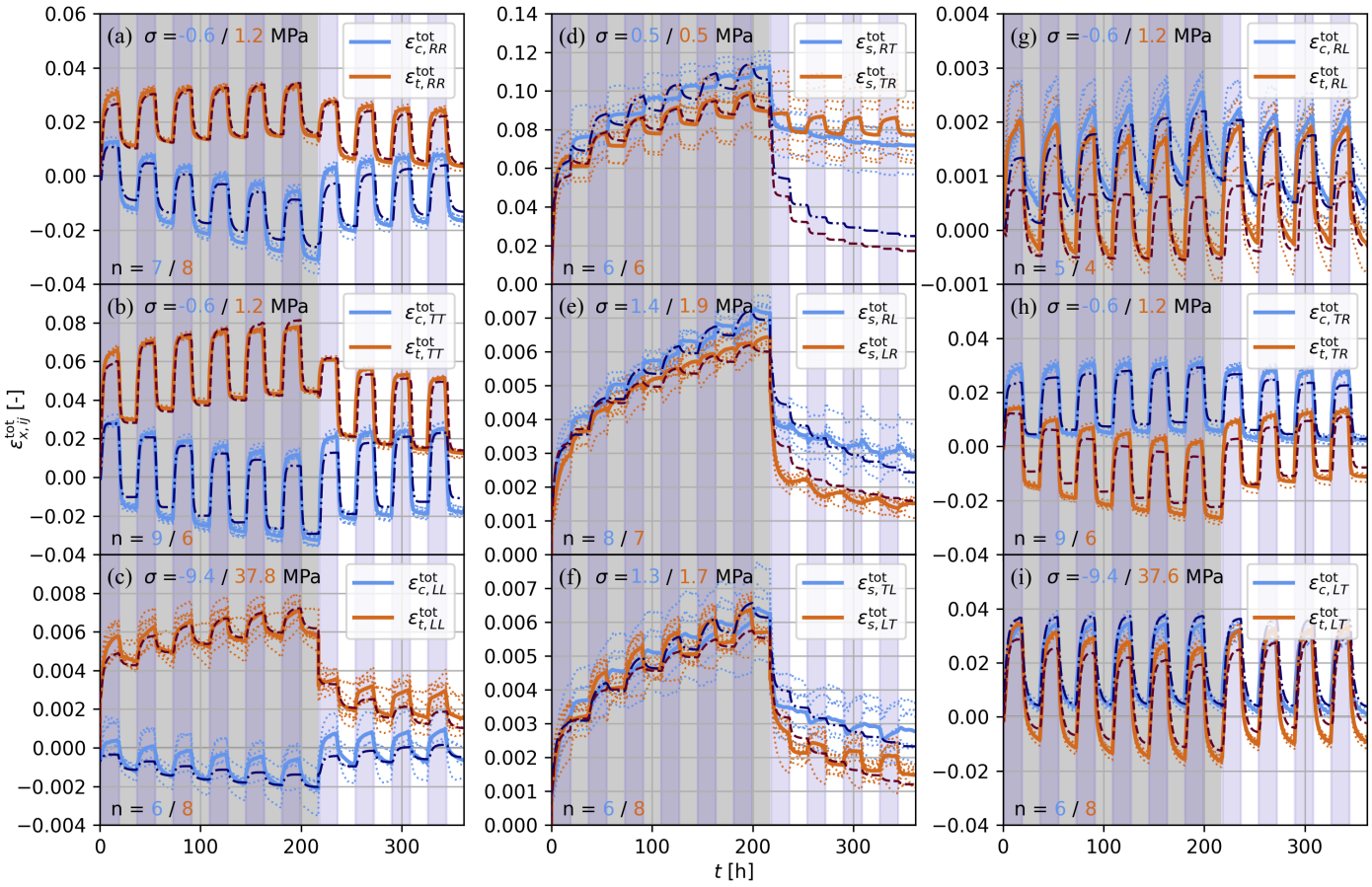


Figure 6: Experimental and simulated strain responses $\epsilon^{\text{tot}}_{\text{x,ij}}$ over time t. Subscript x specifies load type (compression c, tension t, shear s). Subscripts ij denote the loading (i) and strain (j) directions, or the shear plane normal (i) and loading direction (j). Dotted colored lines show individual sample responses (sample count n), solid colored lines show the experimental average, and dashed/dashed-dotted lines plot the model response. Grey and light-purple backgrounds indicate periods under applied stress σ (see Tab. 1 for the corresponding LD) and high-moisture climates, respectively.

nonuniform stress and moisture fields. Hence, the MS parameters are fitted using a hygromechanical FE model to account for these inhomogeneities. The model is subjected to the experimental climate conditions, shown in Fig. 5. Here, φ denotes the measured RH in the creep rack, while ω_{eq} is the corresponding equilibrium MC, applied to the FE model's outer surface through a surface film condition. Equivalent to Sec. 2.2, φ is transformed into ω_{eq} by linearly scaling the sorption isotherm by Maas and Wittel (2026a) such that it equals the creep samples' equilibrium MCs at 35 % and 90 % RH. The applied climate reaches the target climate quickly and exhibits high reproducibility across experiments.

The moisture variations cause pronounced MS creep and hygroexpansion, visible in the total strain response $\epsilon^{\text{tot}}_{x,ij}(t)$ in Fig. 6. Here, x denotes the load type (compression c, tension t, shear s), and ij describes the load direction i and strain direction j for uniaxial tests, and the shear plane normal i and the load direction j for shear tests. The colored dotted lines represent the experimental strain evolution per test, the solid lines their average per time point, and the darker dashed and dashed-dotted lines the strain response of the fitted model (Fig. 3). n is the number of tested specimens and σ is the applied stress.

The experimental strain evolutions show pronounced creep and, except for $\epsilon^{\text{tot}}_{s,TR}$ (Fig. 3.2d), relaxation. The largest strain change always occurs at the first moisture cycle after load application or removal. The R (Figs. 6a, h), T (Figs. 6b, i), and RT/TR shear strains (Fig. 6d) are one magnitude higher than the other components. R and T compression have similar strain magnitudes to tension, even though the applied loads are lower (Figs. 6a, b). Similarly, RL and TL shear strains are similar to their complementary counterparts, despite differing loads (Figs. 6e, f). In general, the experimental R and T strains (Figs. 6a, b, h, i) show low variation between the specimens, while smaller strains in the L direction (Figs. 6c, g) result in a larger scatter due to their lower strain magnitude and an associated lower relative measurement accuracy. The shear strains (Figs. 6d-f) partly show pronounced scatter as well, potentially caused by varying clamping stiffness and, thus, varying rigidity in the mount points of the Arcan sample holder.

The agreement between the model and the total strain

Table 2: Fitted ratio $\Gamma^{(k)}_{x,ij}$ (Eq. 6) of the mechanosorptive compliance of the k-th Kelvin-Voigt element to the elastic compliance for $\boldsymbol{\mu} = [10, 50, 250]\,\%$, with load type x and strain direction ij.

$\epsilon^{\mathrm{ms}}_{x,ij}$	$\Gamma^{(1)}_{x,ij}$ [-]	$\Gamma^{(2)}_{x,ij}$ [-]	$\Gamma^{(3)}_{x,ij}$ [-]
$\epsilon^{\mathrm{ms}}_{c,RR}$	3.0216	1.1814	29.0327
$\epsilon^{\mathrm{ms}}_{t,RR}$	4.8394	0.9949	8.3582
$\epsilon^{\mathrm{ms}}_{c,RR} \cup \epsilon^{\mathrm{ms}}_{t,RR}$	3.9305	1.0881	18.6955
$\epsilon^{\mathrm{ms}}_{c,TT}$	6.9149	5.3234	51.0883
$\epsilon^{\mathrm{ms}}_{t,TT}$	8.0823	0.2645	14.3256
$\epsilon^{\mathrm{ms}}_{c,TT} \cup \epsilon^{\mathrm{ms}}_{t,TT}$	7.4986	2.7939	32.7069
$\epsilon^{\mathrm{ms}}_{c,LL}$	0.0001	1.1597	1.6127
$\epsilon^{\mathrm{ms}}_{t,LL}$	0.2883	0.5584	0.8955
$\epsilon^{\mathrm{ms}}_{c,LL} \cup \epsilon^{\mathrm{ms}}_{t,LL}$	0.1442	0.8590	1.2541
$\epsilon^{\mathrm{ms}}_{c,RL}$	3.0312	7.7108	49.5816
$\epsilon^{\mathrm{ms}}_{t,RL}$	0.0001	0.4394	0.0001
$\epsilon^{\mathrm{ms}}_{c,RL} \cup \epsilon^{\mathrm{ms}}_{t,RL}$	1.5157	4.0751	24.7909
$\epsilon^{\mathrm{ms}}_{c,TR}$	4.7403	16.1414	31.4494
$\epsilon^{\mathrm{ms}}_{t,TR}$	3.5003	7.7155	15.1500
$\epsilon^{\mathrm{ms}}_{c,TR} \cup \epsilon^{\mathrm{ms}}_{t,TR}$	4.1203	11.9284	23.2997
$\epsilon^{\mathrm{ms}}_{c,LT}$	0.0001	0.0001	0.0001
$\epsilon^{\mathrm{ms}}_{t,LT}$	2.5087	0.7005	10.2592
$\epsilon^{\mathrm{ms}}_{c,LT} \cup \epsilon^{\mathrm{ms}}_{t,LT}$	1.2544	0.3503	5.1296
$\epsilon^{\mathrm{ms}}_{s,RT}$	3.9887	0.2986	6.0139
$\epsilon^{\mathrm{ms}}_{s,TR}$	4.8500	0.8603	4.3527
$\epsilon^{\mathrm{ms}}_{s,RT} \cup \epsilon^{\mathrm{ms}}_{s,TR}$	4.4193	0.5795	5.1833
$\epsilon^{\mathrm{ms}}_{s,RL}$	0.8341	0.6403	4.6644
$\epsilon^{\mathrm{ms}}_{s,LR}$	2.0714	0.2799	5.1367
$\epsilon^{\mathrm{ms}}_{s,RL} \cup \epsilon^{\mathrm{ms}}_{s,LR}$	1.4528	0.4601	4.9006
$\epsilon^{\mathrm{ms}}_{s,TL}$	0.7895	0.1252	5.5868
$\epsilon^{\mathrm{ms}}_{s,LT}$	1.6501	2.2594	4.2104
$\epsilon^{\mathrm{ms}}_{s,TL} \cup \epsilon^{\mathrm{ms}}_{s,LT}$	1.2198	1.1923	4.8986

curves is good for most strain components. Exceptions occur in Figs. 6c and g, where the experimental hygroexpansion exceeds the model response. To isolate the mechanical response from hygroexpansion, the model is fitted here only to the experimental strains recorded at 35 % RH. This corresponds to the constant climate maintained during the start, loading, and unloading phases. Further model inaccuracies appear for rolling shear in Fig. 6d, where the signal is only fitted to the loading phase of the deformation curve. Here, the experimental recovery is considerably smaller than the model, indicating larger plastic deformations in the experiments than the model predicts.

The fitted model uses three MS KV elements with $\boldsymbol{\mu} = [10, 50, 250]\,\%$, with their $\boldsymbol{\Gamma}_k$ documented in Tab. 2. The minimum and maximum μ_k were manually chosen to represent the range of moisture changes throughout the experiments and a limited extrapolation range, while a Fisher test (Hajikarimi and Moghadas Nejad, 2021) identified the number of required elements when determining the initial guess of $\boldsymbol{\Gamma}_k$ (see Sec. 2.3).

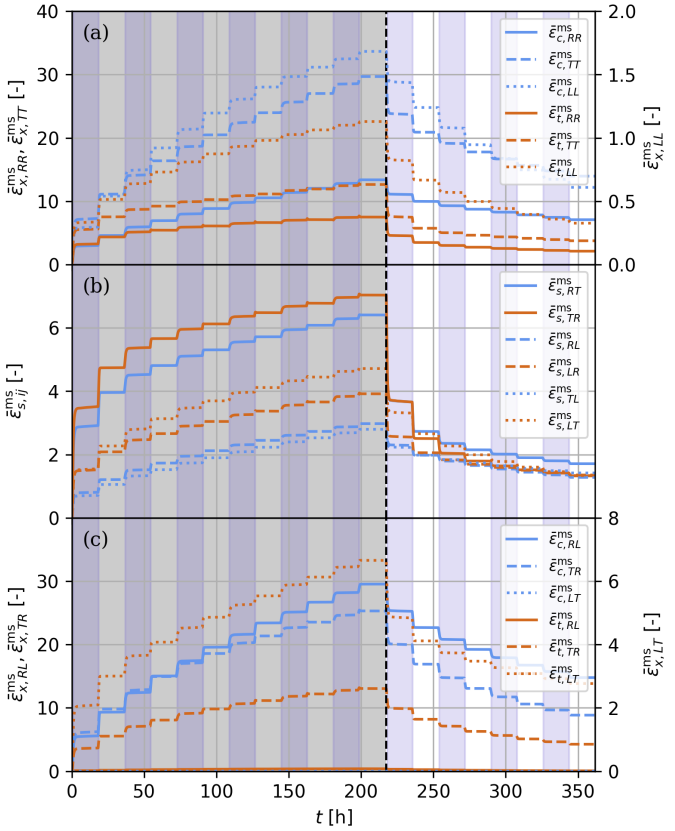


Figure 7: Axial (a), shear (b), and lateral (c) strain responses $\bar{\epsilon}^{\mathrm{ms}}_{x,ij} = \epsilon^{\mathrm{ms}}_{x,ij}/\epsilon^{\mathrm{el}}_{x,ij}(\omega = 19.5\,\%)$ of the fitted mechanosorptive model in a material point under 1 MPa load. The gray and light-purple backgrounds indicate loading periods and high-moisture climates, respectively. The vertical black dashed line marks the unloading. Note that the scales for L tests are on the right y-axes.

3.3. Mechanosorptive strain relations

So far, only total strains have been shown, which do not allow direct comparison of MS behavior across anatomical directions because stress levels differ between tests. Since the rheological model has already been fitted to the data (see Sec. 3.2), one can now study the mechanosorptive response under comparable stress states. Fig. 7 illustrates the MS strain enhancement $\bar{\epsilon}^{\mathrm{ms}}_{x,ij}$ of the fitted MS model (Eq. 5) defined as the ratio between MS and elastic strain $\epsilon^{\mathrm{ms}}_{x,ij}/\epsilon^{\mathrm{el}}_{x,ij}(\omega = 19.5\,\%)$ at the upper moisture level. Note that this strain scaling is in line with Fortino et al. (2009); Hassani et al. (2015); Yu et al. (2022). For comparison, the behavior is evaluated at a material point under a load of 1 MPa in the respective anatomical direction using the same climate history as in Fig. 5.

The normalization highlights that the MS strains can greatly exceed the elastic strains. MS creep in the R and T directions is significantly higher than creep in the grain direction, with compressive MS always exceeding the tensile one (Fig. 7a). When it comes to shear, the MS strain is one order of magnitude closer to the elastic one, as shown in Fig. 7b. The normalized shear deformations for rolling shear are larger than for the other shear compo-

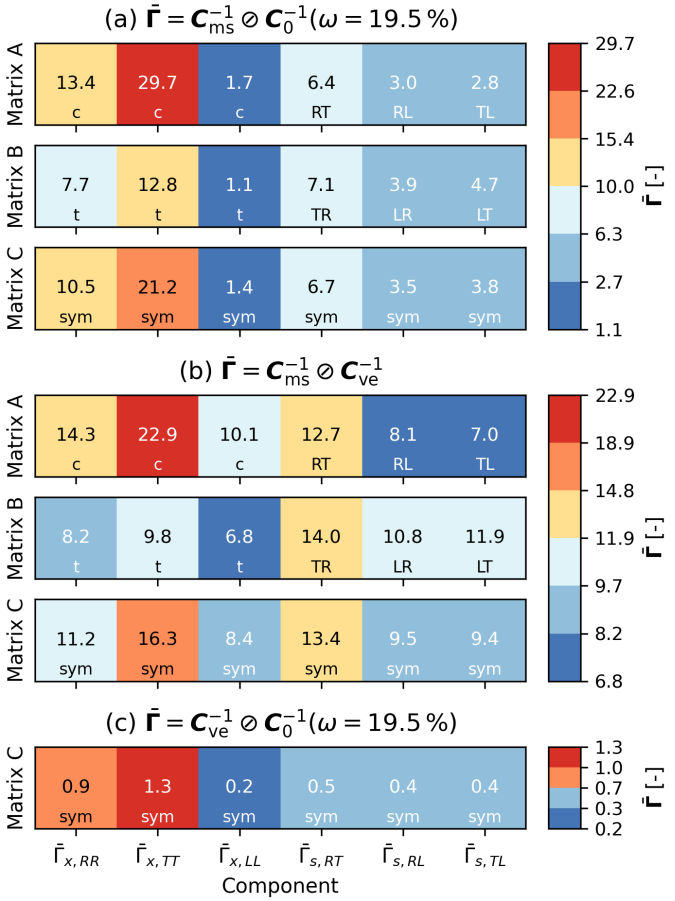


Figure 8: Ratio of the diagonal terms of the mechanosorptive creep compliance $\boldsymbol{C}_{\mathrm{ms}}^{-1}$ before unloading (black dashed line in Fig. 7) to (a) the elastic compliance $\boldsymbol{C}_0^{-1}$ and (b) the viscoelastic creep compliance $\boldsymbol{C}_{\mathrm{ve}}^{-1}$, together with the ratio (c) of $\boldsymbol{C}_{\mathrm{ve}}^{-1}$ to $\boldsymbol{C}_0^{-1}$. *Matrix A* corresponds to the compression and RT, RL, and TL shear components, *matrix B* to the tension and TR, LR, and LT shear components, and *matrix C* to their average.

nents. Rolling shear shows nearly no asymmetry between complementary shear planes, while for the other planes relative MS creep is greater when the stress acts perpendicular to the L direction. To complete the picture, Fig. 7c shows lateral strains. For loading in the R and T directions, lateral MS is larger for compression than tension, whereas the opposite is true for the L direction. However, the large values of $\bar{\epsilon}_{c,RL}$ might arise from measurement inaccuracies, as errors in tiny strains beyond the creep rack's accuracy impact the calculation.

If MS orthotropy followed the elastic one, all lines in Fig. 7 would collapse to a single master curve. Obviously, this is not the case. So the next logical step is to suspect proportionality to viscoelasticity, since MS creep activates similar dissipation mechanisms in cell walls. To clarify this point, Fig. 8 compares the diagonal components of the model's MS creep compliance $\boldsymbol{C}_{\mathrm{ms}}^{-1}$ just before unloading (see black dashed line in Fig. 7) to the elastic and viscoelastic compliance $\boldsymbol{C}_{\mathrm{ve}}^{-1}$ after the same MC evolution. For completeness, the figure also includes the ratio of the viscoelastic to the elastic compliance. The matrix structure follows Eq. 6. *Matrix A* contains the components of the compression tests and the RT, RL, and TL shear planes, while *matrix B* contains the components of the tension tests and the TR, LR, and LT shear planes. *Matrix C* is the resulting matrix obtained by component-wise averaging, i.e., symmetrizing matrices A and B. The viscoelastic compliance is calculated using Eqs. A.3 and A.4. Note that only the diagonal entries are compared, as they are more significant for the overall strain response. Unfortunately, Figs. 8a and b show that the MS compliance is neither proportional to the elastic compliance nor to the viscoelastic compliance. However, one can assess the differences in the scaling factors. For example, one may identify, for scaling of *matrix C* with the elastic compliance (Fig. 8a), that the RL/LR and TL/LT shear directions are similar. Equivalently, one can group the RL/LR and TL/LT shear directions with the L direction for viscoelastic scaling (Fig. 8 b). Scaling groups can also be identified between the viscoelastic and elastic compliance (Fig. 7c). To summarize, MS cannot be derived from a proportional scaling of the viscoelastic compliance matrix, but scaling groups among compliances or their combinations may reduce the number of cases required for material characterization.

4. Discussion

This study provides a full, consistent orthotropic picture for wood mechanosorption. It is complemented by an investigation of asymmetries between compression and tension, as well as between complementary shear planes. Such completeness enables future MS models to accurately account for the significant orthotropic differences that previous models had to ignore due to a lack of experimental knowledge. As MS is the largest contributor to wood deformation under varying environmental conditions, this will considerably improve predictions for wood structural behavior. Fitting MS with a constitutive model in which all rheological parameters are derived from experiments on samples from the same tree yields exceptionally high parameter consistency. Sec. 4.1 discusses the general validity of the diffusion coefficients, which were optimized to predict MC evolution in the creep samples. Subsequently, Sec. 4.2 evaluates the observed MS behavior, the general applicability of the MS parameters, and what the results imply for future MS models. Finally, Sec. 4.3 discusses how the FE model's boundary conditions affect the predicted shear strains, which, for rolling shear, are considerably smaller than the experimentally observed irrecoverable deformations.

4.1. Validity of diffusion coefficients

The goal of the sorption experiments was not to determine general diffusion coefficients, but to accurately predict the moisture field within the creep samples. Hence, the moisture-transport model was optimized to replicate the

MC evolution of samples with identical dimensions. To reduce the number of interdependent variables, the moisture dependence of the surface film coefficient was neglected. Although calibrated to a single specific geometry, the diffusion parameters $D_{0,R}$, $D_{0,T}$, α_R, and α_T are similar to the values used by Hanhijärvi (1995), which are applied in several hygromechanical wood models (e.g. Saft and Kaliske, 2011; Hassani et al., 2015). Furthermore, the increase of D_R and D_T over MC (Kübler, 1957; Sonderegger et al., 2011; Koumoutsakos and Avramidis, 2002), and the corresponding decrease of D_L (Kübler, 1957; Koumoutsakos and Avramidis, 2002; Perkowski et al., 2017), are consistent with other studies investigating conifers. The magnitude of D_L is similar to values reported by Sonderegger et al. (2011), but it does not represent the bulk material, as the samples are only 4 mm thick. With tracheid length in Norway spruce ranging from 2 mm to 4 mm (Pyörälä et al., 2022), the tested samples contain at most two complete layers of tracheids across their thickness, leaving moisture transport strongly influenced by different transport pathways. Hence, the determined coefficients are reasonable in magnitude but specific to the sample geometry because of pronounced boundary effects.

4.2. Applicability of mechanosorptive parameters

Wood under changing moisture is always subjected to nonuniform moisture and stress fields. Numerous studies investigating MS (e.g. Ranta-Maunus, 1975; Svensson and Toratti, 2002; Saifouni et al., 2016; Peng et al., 2020) neglect these inhomogeneities and instead determine MS using 1D continuous models. However, because MS creep rates vary across the nonuniform stress field, these results are not representative of the material and have limited reproducibility beyond the tested samples. Fig. 9a shows, exemplarily for T compression samples, R stresses after the start of the first moisture cycle. The dry inner cross-section prevents the outer, moist surface from expanding, causing tension in the center and compression at the outer surface. Throughout the load and moisture history, such tension and compression zones cause creep and plastic strains to evolve non-monotonously (see Fig. 9b) and inhomogeneously, resulting in complex stress fields with frozen strain components. As these internal stresses and components notably affect the sample's overall strain response, they must be considered for correctly assessing MS parameters, as, e.g., in Huč et al. (2018) or Florisson et al. (2021).

The experimental scope of the present study aims to identify full MS creep orthotropy and the corresponding load asymmetries. The strain responses of the corresponding creep experiments align qualitatively with other studies and confirm that MS can exceed elasticity by more than a magnitude (Svensson and Toratti, 2002). Quantitatively, the magnitude of MS creep in the L direction is comparable to other studies (Bengtsson, 1999, 2001), but more than doubled for tension in the R and T directions (Froidevaux et al., 2012; Ferrara and Wittel, 2026a) and for compression perpendicular to the grain (Massaro and Malo, 2019). However, Froidevaux et al. (2012) and Massaro and Malo (2019) conducted moisture cycles at lower RH, and Ferrara and Wittel (2026a) tested very thin cross-sections. This highlights that the upper moisture level strongly influences MS, consistent with Liu (1993), and that size effects influence the MS creep response. The fact that compression creep is significantly larger than tension creep has also been observed in other studies (Armstrong and Christensen, 1961; Bengtsson, 1999; Toratti and Svensson, 2000; Strömbro and Gudmundson, 2008). It may relate to cell wall bulging under compression, but a micromechanical explanation remains missing to date.

The observed MS creep orthotropy, where $\epsilon^{\mathrm{ms}}_{x,TT} > \epsilon^{\mathrm{ms}}_{x,RR} \gg \epsilon^{\mathrm{ms}}_{x,LL}$ is consistent with Peng et al. (2019) and Peng et al. (2020) and similar to viscoelasticity (Maas and Wittel, 2025; Ferrara and Wittel, 2025). While the low MS in the L direction can be attributed to load alignment with the microfibril angle and a homogeneous stress distribution across the full tracheid cross-section, differences between the R and T directions may reflect nonlinear deformations at stress-concentration points within the cell walls (Ferrara and Wittel, 2026b). As Maas and Wittel (2025) highlight, cell-wall deformations during T creep are bending-dominated, while the load paths for R creep align within the T cell walls. Bending induces stress concentrations near cell-wall corners, resulting in high local LDs and nonlinear deformations that ultimately yield a larger macroscopic creep response than in the R direction, where no such stress localizations occur.

The orthotropy of the elastic or viscoelastic compliance matrices cannot account for the MS orthotropy, as

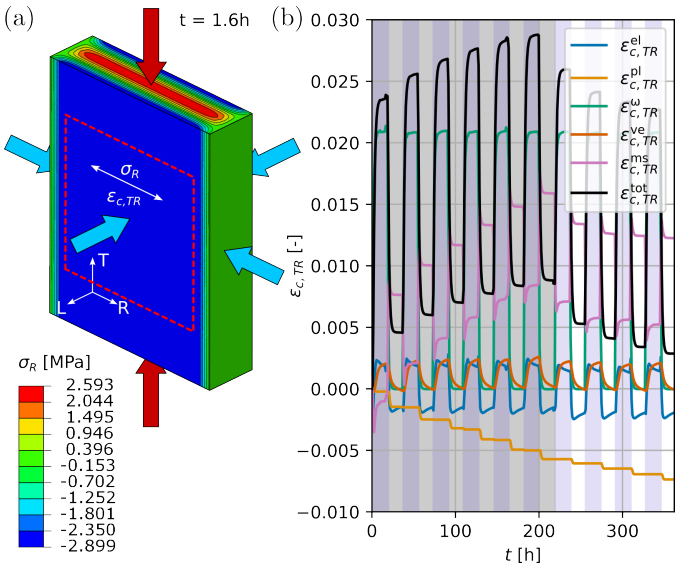


Figure 9: (a) Simulated radial stress field σ_R of T compression tests after beginning the first moistening cycle. The red arrows denote the loading direction, blue arrows show the moisture flow, and the red dashed line highlights the averaging region for strains. (b) Evolution of corresponding strains $\epsilon_{c,TR}$ over time t. Shaded areas denote loading (gray) and moist climates (blue).

no unified proportionality was found among the components. Hence, proportional scaling based on elastic (as in Fortino et al., 2009; Hassani et al., 2015; Yu et al., 2022) or viscoelastic compliance (as in Stöcklein et al., 2024) yields incorrect results. To reduce experimental effort, the component ratios in this paper can be used to scale missing data. Obviously, those ratios depend on anatomic features and may vary between trees and species. Nevertheless, this approach will yield better results than proportional elastic or viscoelastic scaling. We recommend testing the most dissimilar stress states identified in Fig. 8.

The data originate from defect-free sections of a single tree. Consequently, variations in density and structure were not addressed. Furthermore, MS was determined only for a single large MC amplitude and one constant LD. For lower MC ranges, the MS creep might be significantly smaller (Liu, 1993). The off-diagonal terms for the R and L uniaxial tests are less robust due to their low strain magnitudes, and their ratios to elastic and viscoelastic compliances must be interpreted with caution. However, these components contribute only a small amount to the overall strain response. Furthermore, the model considers only plasticity and no other damage mechanisms, and it decomposes the strain components using an additive model. Potential coupling effects between rheological mechanisms are not considered. Unfortunately, this study cannot provide an error estimate for the determined MS parameters because of uncertainty in all model parameters, highly nonlinear coupling among them, experimental uncertainties, model simplifications, nonlinear stress and moisture fields, gradient-free fitting methods, and long computational times. Lastly, the large scatter in shear sample responses suggests that Arcan sample holders may not be ideal for MS tests due to constrained swelling, and future MS shear tests may benefit from an improved test setup.

4.3. Influence of boundary conditions

The observed rolling shear strains show considerable permanent deformation that the FE model does not capture. The model's response depends strongly on the applied boundary conditions, which should ideally match the experiments as closely as possible. However, these boundary conditions are not well defined for the Arcan tests. Figs. 10a and b show that as MC increases, the sample swells horizontally. The samples partly slip within the sample holder, but are also partly constrained. This causes horizontal compression in the evaluated cross-section at high RHs, resulting in a multiaxial stress state with increased shear plasticity. Figs. 10c and d compare the extreme cases of this mixed stress state, i.e., frictionless horizontal movement vs. fully horizontal constraint of the model's right boundary surface (Fig. 3c). Visibly, even the fully constrained model cannot reproduce the magnitude of irrecoverable deformation observed in the experiments. This suggests that plastic rolling-shear deformation during moisture cycles is considerably larger than the plastic deformation at

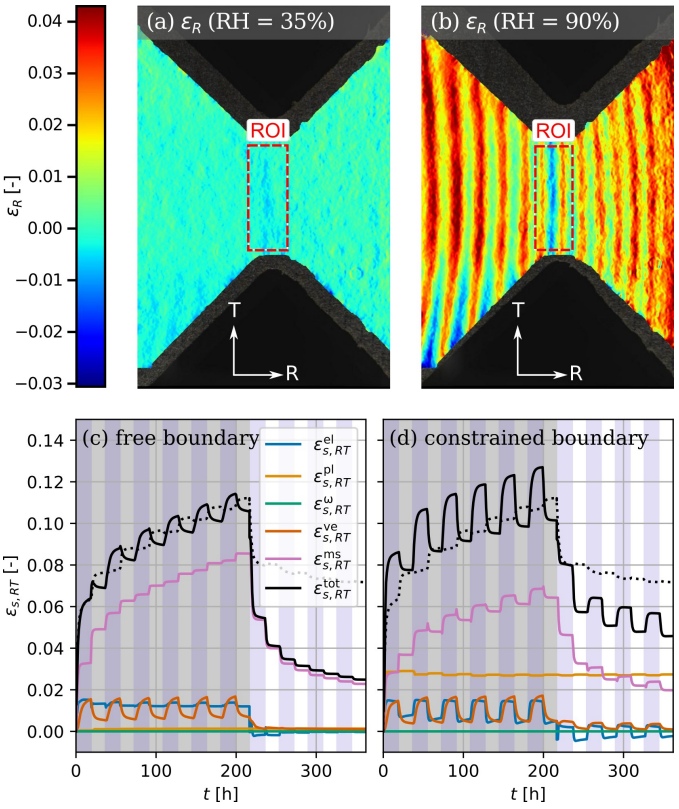


Figure 10: Influence of the clamping boundary conditions on the shear strain field. (a) Horizontal strains after load application before the first moistening. (b) Horizontal strain at the end of the first moistening, causing compression stresses in the R direction. (c) and (d) show the evolution of the shear strain $\epsilon_{s,RT}$ over time t of the fitted FE model under boundary conditions that respectively enable/constrain the horizontal movement of the sample within the sample holder. The solid lines represent the fitted model's strain components, while the dotted line represents the experimental strains.

90 % RH, which the present model captures. Hence, a separate consideration of irrecoverable MS, as in Fortino et al. (2009), might be applicable. Note that the fully constrained model was not applicable for fitting due to substantially longer computation times. However, as the total strains in Figs. 10c and d are similar during the loading phase, the 'true' shear creep parameters for the mixed boundary conditions are expected to be similar to the fitted creep coefficients.

To enable a clean assessment of MS shear creep, future experiments should allow for free swelling and shrinkage to ensure clean stress states and well-defined boundary conditions. This is especially relevant for rolling shear, which, unlike the other shear planes, experiences pronounced plastic flow (Maas and Wittel, 2026a), which might increase under multiaxial stress states. Nevertheless, the parameters in the present study yield a better approximation than scaling shear MS by the R or T compliances, which are considerably larger and of different magnitude.

5. Conclusions

This work provides a comprehensive overview of the orthotropy and load asymmetry of wood MS. Fully identifying orthotropy, scaling relationships, and relevant loading-direction dependencies reveals weaknesses in contemporary wood models and yields a complete set of orthotropic MS parameters. The identified patterns lead to the following recommendation for improving future MS models of wood:

- MS creep is highly orthotropic and not proportional to the elastic and viscoelastic compliances. However, the components group into scaling clusters. Hence, experimental data should be provided for the most dissimilar anatomical directions, while similar components can be scaled.
- In the R and T directions, compression MS can be several times larger than tension MS. Because these large differences affect stress distributions in simulation models (e.g., bending beams), compression and tension should be treated separately.
- MS rolling shear has a larger scaling ratio with respect to the elastic and viscoelastic compliances than the other shear components, with considerable irrecoverable deformation that pure plasticity cannot explain. The other shear planes do not show such irrecoverable strains, and their MS creep is slightly larger for forces perpendicular to the grain than parallel to it.
- Changing moisture cycles create severe, non-uniform, history-dependent moisture and stress fields within the samples, which hygromechanical models and MS parameter measurements must account for.

Because MS creep is, by nature, the part of the strain that cannot be explained by other deformation mechanisms (viscoelastic, plastic, hygroexpansion, and elastic), it depends strongly on a correct understanding and implementation of those mechanisms in constitutive models. Hence, it must always be regarded within a given constitutive model framework. Using the consistent experimental insights, the blind spots in our rheological model by Hassani et al. (2015) could be removed by improving the orthotropic moisture-dependent plasticity, viscoelasticity, and mechanosorptivity. With the consistent spruce dataset provided (Maas and Wittel, 2026c,b) (see also Data Availability Statement), we give a model-free basis for other researchers to apply and improve their own constitutive model implementations.

Future studies could investigate a systematic assessment of LD dependencies, the nonlinear influence of absolute MC, shear MS under free hygroexpansion, and the role of load and moisture history on the MS strain response. Furthermore, the transferability of the orthotropic MS ratios to other wood species would be of great interest.

Appendix A. Simulation model parameters

This study uses the Abaqus User Material (UMAT) developed by Hassani et al. (2015) to decompose the mechano-sorptive tests' total strains into their respective components. The UMAT was updated with the material parameters reported by Maas and Wittel (2026a), which originate from the same tree as the samples in the present study. This appendix describes all incorporated changes and formulations of strain calculation.

The UMAT uses a moisture-dependent orthotropic material formulation in Voigt notation with strain vector $\boldsymbol{\epsilon} = [\epsilon_\mathrm{R} \quad \epsilon_\mathrm{T} \quad \epsilon_\mathrm{L} \quad \epsilon_\mathrm{RT} \quad \epsilon_\mathrm{RL} \quad \epsilon_\mathrm{TL}]^\top$ and stress vector $\boldsymbol{\sigma} = [\sigma_\mathrm{R} \quad \sigma_\mathrm{T} \quad \sigma_\mathrm{L} \quad \sigma_\mathrm{RT} \quad \sigma_\mathrm{RL} \quad \sigma_\mathrm{TL}]^\top$. The subscripts denote the anatomical direction, i.e., radial (R), tangential (T), and longitudinal (L). One subscript i indicates the normal direction, whereas two subscripts ij indicate the shear component for a shear normal to i caused by a force in direction j.

The elastic strains $\boldsymbol{\epsilon}^\mathrm{el}$ are calculated by Hooke's law via

$$\boldsymbol{\epsilon}^\mathrm{el}(\omega) = \boldsymbol{C}_0^{-1}(\omega) \cdot \boldsymbol{\sigma}. \tag{A.1}$$

$\boldsymbol{C}_0^{-1}(\omega)$ is the moisture-dependent compliance matrix, $\boldsymbol{\sigma}$ the applied stress, and ω the moisture content (MC). Tab. A.1 documents the formulation of all symmetrized non-zero components of $\boldsymbol{C}_0^{-1}(\omega)$.

The hygroexpansive strain increments $\dot{\boldsymbol{\epsilon}}^\omega$ are calculated as proportional to the MC increment $\dot{\omega}$

$$\dot{\boldsymbol{\epsilon}}^\omega = \boldsymbol{\alpha} \cdot \dot{\omega}. \tag{A.2}$$

$\boldsymbol{\alpha} = [\alpha_R \quad \alpha_T \quad \alpha_L \quad 0 \quad 0 \quad 0]^\top$ are the hygroexpansion coefficients, with $\alpha_R = 0.1816$, $\alpha_T = 0.3425$, and $\alpha_L = 0.0061$.

The viscoelastic strains $\boldsymbol{\epsilon}^\mathrm{ve}$ are calculated with a Kelvin-Voigt model with $n = 4$ elements with fixed characteristic times $\boldsymbol{\tau} = [2\,\mathrm{h} \quad 20\,\mathrm{h} \quad 200\,\mathrm{h} \quad 2000\,\mathrm{h}]$. The strain increment $\dot{\boldsymbol{\epsilon}}^\mathrm{ve}$ is

$$\dot{\boldsymbol{\epsilon}}^\mathrm{ve}(t,\omega) = \sum_m^n \frac{1}{\tau_m} \left(\boldsymbol{C}_m^{-1}(\omega) \cdot \boldsymbol{\sigma}(t) - \boldsymbol{\epsilon}_m^\mathrm{ve}(t,\omega) \right). \tag{A.3}$$

Table A.1: Non-zero elastic compliance components $C_{0,ij}^{-1}(\omega) = 1/(p_{0,ij}^\mathrm{el}\omega^2 + p_{1,ij}^\mathrm{el})$ at moisture content ω.

ij	$p_{0,ij}^\mathrm{el}$ [MPa/%^{2}]	$p_{1,ij}^\mathrm{el}$ [MPa]
11	−1.1687	1280.04
22	−0.4484	731.93
33	−4.1716	13972.72
44	−0.0181	55.16
55	−0.9967	1506.38
66	−1.3058	1750.87
12, 21	2.9720	−2696.82
13, 31	9.9158	−29169.71
23, 32	14.9514	−25056.28

Table A.2: Non-zero relative viscoelastic compliance components $G_{m,ij}$ for the m-th Kelvin-Voigt element at moisture content $\omega = 0\,\%$.

ij	$G_{1,ij}$ [−]	$G_{2,ij}$ [−]	$G_{3,ij}$ [−]	$G_{4,ij}$ [−]
11	0.1829	0.2863	0.2816	0.5989
22	0.4121	0.2820	0.6030	0.3500
33	0.0669	0.0293	0.0793	0.1261
44	0.1920	0.1088	0.0785	0.1400
55	0.1813	0.0658	0.1726	0.3261
66	0.1539	0.0966	0.1706	0.2996
12, 21	0.0994	0.2517	0.3771	0.4692
13, 31	0.5237	0.5606	1.0370	1.2254
23, 32	0.0360	0.0881	0.3397	0.0878

Table A.3: Non-zero viscoelastic multiplication factors $\phi_{ij}(\omega) = 1 + (p^{\mathrm{ve}}_{0,ij} - 1)/(1 + \exp(-p^{\mathrm{ve}}_{1,ij}(\omega - p^{\mathrm{ve}}_{2,ij})))$ at moisture content ω.

ij	$p^{\mathrm{ve}}_{0,ij}$ [−]	$p^{\mathrm{ve}}_{1,ij}$ [1/%]	$p^{\mathrm{ve}}_{2,ij}$ [%]
11	3.8327	1.1374	18.6247
22	2.7600	1.1480	18.6170
33	2.0321	1.0364	19.6214
44	4.8229	1.3036	18.5836
55	2.0027	1.0292	19.5990
66	2.7126	1.1108	19.3425
12, 21	3.9074	1.1899	17.8518
13, 31	2.3936	1.2334	19.7517
23, 32	13.8628	1.4960	19.7985

m denotes the index of the Kelvin-Voigt element and $\boldsymbol{C}_m^{-1}(\omega)$ the corresponding characteristic compliance matrix, which is calculated as:

$$\boldsymbol{C}_m^{-1}(\omega) = \boldsymbol{G}_m \circ \boldsymbol{C}_0^{-1}(\omega) \circ \boldsymbol{\phi}(\omega). \tag{A.4}$$

$\boldsymbol{G}_m$ is the relative characteristic compliance of the m-th Kelvin-Voigt element at $\omega = 0\,\%$, $\boldsymbol{C}_0^{-1}(\omega)$ the moisture-dependent elastic compliance matrix, $\boldsymbol{\phi}(\omega)$ a moisture-dependent multiplication matrix, and $\circ$ denotes the element-wise product. $\boldsymbol{G}_m$ and $\boldsymbol{\phi}(\omega)$ are derived from a least-squares fitting of the utilized Kelvin-Voigt series over the moisture-dependent viscoelastic creep data in Maas and Wittel (2026a). As in the original data, moisture dependence is expressed as a logistic function. Tabs. A.2 and A.3 document the non-zero components of $\boldsymbol{G}_m$ and $\boldsymbol{\phi}$, respectively.

A multi-surface plasticity model with isotropic hardening calculates the plastic strains. It uses two yield surfaces for R and T compression and, unlike Hassani et al. (2015), one yield surface for rolling shear rather than L compression. In Maas and Wittel (2026a), these anatomical directions show the most pronounced plastic yielding. Each yield surface f_l in direction l is described as

$$f_l(\boldsymbol{\sigma}, \alpha_l, \omega) = \boldsymbol{a}_l(\omega) \cdot \boldsymbol{\sigma} + \boldsymbol{\sigma}^\top \cdot \boldsymbol{b}(\omega) \cdot \boldsymbol{\sigma} + q_l(\alpha_l, \omega) - 1. \tag{A.5}$$

$\boldsymbol{a}_l$ and $\boldsymbol{b}_l$ are the strength tensors, q_l the hardening function, and α_l the internal hardening variable in direction $l \in \{R, T, RT\}$. The strength tensors are

Table A.4: Yield strengths $f_{x,l}(\omega) = K \cdot \hat{\epsilon}^{1/n} \cdot (p^{\mathrm{f}}_0 \omega + p^{\mathrm{f}}_1)$ at offset plastic strain $\hat{\epsilon} = 2 \cdot 10^{-4}$ and moisture content ω.

	K [−]	n [−]	p^{f}_0 [MPa/%]	p^{f}_1 [MPa]
$f_{c,R}$	1.111	43.917	−0.121	5.96
$f_{c,T}$	1.803	7.977	−0.194	8.41
$f_{c,L}$	1.952	10.752	−1.872	67.18
$f_{t,L}$	4.685	4.072	−1.600	153.87
$f_{s,RT}$	2.797	4.272	−0.008	1.43
$f_{s,TR}$	2.043	4.600	−0.022	2.20
$f_{s,RL}$	3.258	5.958	−0.182	8.20
$f_{s,LR}$	2.928	6.228	−0.195	10.47
$f_{s,TL}$	2.435	7.746	−0.188	8.78
$f_{s,LT}$	2.970	6.728	−0.189	10.12

$$\boldsymbol{a}_R = \left[\tfrac{1}{f_{c,R}} \quad 0 \quad 0 \quad 0 \quad 0 \quad 0\right], \tag{A.6}$$

$$\boldsymbol{b}_R = \mathrm{diag}\left[0,\ \frac{0.40}{f_{c,T}^2},\ \frac{-0.25}{f_{c,L} f_{t,L}},\ \frac{0.10}{f_{s,RT} f_{s,TR}},\ \frac{0.33}{f_{s,RL} f_{s,LR}},\ \frac{0.33}{f_{s,TL} f_{s,LT}}\right], \tag{A.7}$$

$$\boldsymbol{a}_T = \left[0 \quad \tfrac{1}{f_{c,T}} \quad 0 \quad 0 \quad 0 \quad 0\right], \tag{A.8}$$

$$\boldsymbol{b}_T = \mathrm{diag}\left[\frac{0.40}{f_{c,R}^2},\ 0,\ \frac{-0.25}{f_{c,L} f_{t,L}},\ \frac{0.10}{f_{s,RT} f_{s,TR}},\ \frac{0.33}{f_{s,RL} f_{s,LR}},\ \frac{0.33}{f_{s,TL} f_{s,LT}}\right], \tag{A.9}$$

$$\boldsymbol{a}_{RT} = \left[\tfrac{-0.20}{f_{c,R}} \quad \tfrac{-0.20}{f_{c,T}} \quad 0 \quad 0 \quad 0 \quad 0\right], \tag{A.10}$$

$$\boldsymbol{b}_{RT} = \mathrm{diag}\left[\frac{0.25}{f_{c,R}^2},\ \frac{0.25}{f_{c,T}^2},\ 0,\ \frac{1}{f_{s,RT} f_{s,TR}},\ 0,\ 0\right]. \tag{A.11}$$

$\boldsymbol{a}_l$ and $\boldsymbol{b}_l$ in R and T compression follow the formulation by Hassani et al. (2015) for Norway spruce, except that the factor in b_{44} was reduced because rolling shear is now represented by its own yield surface. The yield surface formulation for rolling shear follows Schmidt and Kaliske (2006), but omits all components in the RL and TL shear plane, as expected shear plasticity is very low in these planes (Maas and Wittel, 2026a).

$f_{x,l}$ are the moisture-dependent yield strengths for loading type x (compression c, tension t, shear s) in direction l. In the model, they correspond to the stress at an offset plastic strain of 0.02 % and are documented in Tab. A.4. Hardening is proportional to the yield strength $f_{x,l}$ (Maas and Wittel, 2026a) and expressed in the UMAT as (Hassani et al., 2015)

$$q_l(\alpha_l, \omega) = (\beta_{0,l}\omega - \beta_{1,l})(1 - \exp(-\beta_{2,l}\alpha_l))/f_{x,l}. \tag{A.12}$$

$\beta_{i,l}$ are fitting parameters and $f_{x,l}$ is $f_{c,l}$ for $l \in \{R, T\}$ and $f_{s,l}$ for $l = RT$. Tab. A.5 depicts the corresponding

Table A.5: Plastic hardening parameters for $q_l(\alpha_l, \omega)$ (Eq. A.12).

l	$\beta_{0,l}$ [MPa/%]	$\beta_{1,l}$ [MPa]	$\beta_{2,l}$ [−]
R	0.0071	0.4406	118.5245
T	0.0420	2.6578	116.1565
RT	0.0208	5.7096	488.5016

parameters, which a least-squares algorithm fitted to the hardening curves in Maas and Wittel (2026a).

In the original UMAT, the final yield surface was defined as $f = \max\{f_l\}$. Because the resulting f is only C^0 continuous, this may cause numerical instability in stress states near intersections of the yield surfaces. To ensure C^2 continuity and improve numerical stability, the UMAT was updated using the smoothing algorithm developed by Wilkins et al. (2020). The smoothed yield surface f_s for two yield surfaces f_1 and f_2 is

$$f_s(f_1, f_2) = \begin{cases} f_1 & \text{for } f_1 \geq f_2 + a \\ \frac{1}{2}(f_1 + f_2 + a) & \\ \quad + g(f_1 - f_2) & \text{for } |f_1 - f_2| < a \\ f_2 & \text{for } f_2 \geq f_1 + a, \end{cases} \tag{A.13}$$

$$g(x) = -\frac{a}{\pi} \cos \frac{\pi x}{2a}, \tag{A.14}$$

where $a = 0.5$ is a user-defined smoothing parameter and $g(x)$ a smoothing function that satisfies the C^2 condition. The final continuous yield surface f of the model is $f = f_s(f_s(f_R, f_T), f_{RT})$. The UMAT calculates the plastic increments of f using the closest-point projection algorithm from Simo and Hughes (1998, p. 146).

Acknowledgement

The authors gratefully acknowledge Thomas Schnider for his assistance with sample preparation. We also thank Ingo Burgert for his valuable support and Peter Niemz for insightful discussions. We thank P. Neuss and M. Högemann, whose master's projects provided valuable preliminary work on the UMAT update. This work was financially supported by the Swiss National Science Foundation (SNF grant 200021_192186, "Creep behavior of wood on multiple scales").

Data availability

The experimental curves and corresponding model responses are available in a Git repository (Maas and Wittel, 2026c) via Python Jupyter notebooks. The notebooks include interactive widgets for quick data exploration and export. The User Material subroutine is available in a separate repository (Maas and Wittel, 2026b) with a minimal working example in Abaqus.

References

Amando de Barros, J.O., Wittel, F.K., 2026. The role of moisture gradients and time scales in wood mechanosorption. Wood Sci. Technol. 60, 91.

Armstrong, L.D., Christensen, G.N., 1961. Influence of moisture changes on deformation of wood under stress. Nature 191, 869–870.

Barkas, W.W., 1949. The Swelling of Wood under Stress: A Discussion of Its Hygroscopic, Elastic and Plastic Properties. HMSO, London.

Bažant, Z.P., Meiri, S., 1985. Measurements of compression creep of wood at humidity changes. Wood Sci. Technol. 19, 179–182.

Bengtsson, C., 1999. Mechanosorptive creep of wood in tension and compression, in: 1st RILEM Symposium on Timber Engineering, Stockholm. pp. 317–326.

Bengtsson, C., 2001. "short-term" mechano-sorptive creep of well-defined spruce timber. Holz Roh. Werkst. 59, 117–128.

Blaber, J., Adair, B., Antoniou, A., 2015. Ncorr: Open-source 2d digital image correlation Matlab software. Exp. Mech. 55, 1105–1122.

Dassault Systèmes, 2021. Abaqus 2021.HF16. Johnston, RI, USA. Version 2021.HF16.

Entwistle, K.M., Zadoroshnyj, A., 2008. The recovery of mechano-sorptive creep strains. J. Mater. Sci. 43, 967–973.

Ferrara, A., Wittel, F.K., 2025. Tensile creep of Norway spruce on the tissue scale. Mech. Time-Depend. Mater. 29, 36.

Ferrara, A., Wittel, F.K., 2026a. Mechanosorptive creep of Norway spruce on the tissue scale perpendicular to grain. Holzforschung 80, 277–289.

Ferrara, A., Wittel, F.K., 2026b. Orthotropic viscoelastic creep in cellular scaffolds. Acta Mech. 237, 1481–1497.

Florisson, S., Vessby, J., Ormarsson, S., 2021. A three-dimensional numerical analysis of moisture flow in wood and of the wood's hygro-mechanical and visco-elastic behaviour. Wood Sci. Technol. 55, 1269–1304.

Fortino, S., Mirianon, F., Toratti, T., 2009. A 3D moisture-stress FEM analysis for time dependent problems in timber structures. Mech. Time-Depend. Mater. 13, 333–356.

Froidevaux, J., Volkmer, T., Ganne-Chédeville, C., Gril, J., Navi, P., 2012. Viscoelastic behaviour of aged and non-aged spruce wood in the radial direction. Wood Mater. Sci. Eng. 7, 1–12.

Gibson, E.J., 1965. Creep of wood: Role of water and effect of a changing moisture content. Nature 206, 213–215.

Gril, J., 1987. A uniaxial model of wood for hygro-thermo-mechanical loadings, in: Bui, H.D., Nguyen, Q.S. (Eds.), Thermomechanical Couplings in Solids, North-Holland, Amsterdam. pp. 263–276.

Grossman, P.U.A., 1976. Requirements for a model that exhibits mechano-sorptive behaviour. Wood Sci. Technol. 10, 163–168.

Hajikarimi, P., Moghadas Nejad, F., 2021. Applications of Viscoelasticity. 1 ed., Elsevier Ltd., Amsterdam, Netherlands.

Hanhijärvi, A., 1995. Modelling of Creep Deformation Mechanisms in Wood. Doctoral Thesis. VTT. Espoo.

Hanhijärvi, A., Hunt, D., 1998. Experimental indication of interaction between viscoelastic and mechano-sorptive creep. Wood Sci.Technol. 32, 57–70.

Hanhijärvi, A., Mackenzie-Helnwein, P., 2003. Computational analysis of quality reduction during drying of lumber due to irrecoverable deformation. I: Orthotropic viscoelastic-mechanosorptive-plastic material model for the transverse plane of wood. J. Eng. Mech. 129, 996–1005.

Hassani, M.M., Wittel, F.K., Hering, S., Herrmann, H.J., 2015. Rheological model for wood. Comput. Methods Appl. Mech. Eng. 283, 1032–1060.

Hering, S., 2011. Charakterisierung Und Modellierung Der Materialeigenschaften von Rotbuchenholz Zur Simulation von Holzverklebungen. Doctoral Thesis. ETH Zurich.

Huč, S., Svensson, S., Hozjan, T., 2018. Hygro-mechanical analysis of wood subjected to constant mechanical load and varying relative humidity. Holzforschung 72, 863–870.

Hunt, D.G., 1989. Linearity and non-linearity in mechano-sorptive creep of softwood in compression and bending. Wood Sci. Technol. 23, 323–333.

Hunt, D.G., 1999. A unified approach to creep of wood. Proc. Math. Phys. Eng. Sci. 455, 4077–4095.

Kauman, W.G., 1966. On the deformation and setting of the wood cell wall. Holz Roh. Werkst. 24, 551–556.

Koumoutsakos, A., Avramidis, S., 2002. Mass transfer characteristics of western hemlock and western red cedar. Holzforschung 56, 185–190.

Kübler, H., 1957. Studien über die Holzfeuchtebewegung. Holz Roh- Werkst. 15, 453–468.

Leicester, R.H., 1971. A rheological model for mechano-sorptive deflections of beams. Wood Sci. Technol. 5, 211–220.

Liu, T., 1993. Creep of wood under a large span of loads in constant and varying environments. Holz Roh- Werkst. 51, 400–405.

Maas, J.M., Wittel, F.K., 2025. Comprehensive creep compliance characterization of orthotropic materials using an automated system. Holzforschung 79, 116–133.

Maas, J.M., Wittel, F.K., 2026a. From elasticity to creep: Orthotropic moisture-dependent rheology of Norway spruce. Holzforschung 80, 514–542.

Maas, J.M., Wittel, F.K., 2026b. Hygromechanical orthotropic spruce UMAT (version 0.1) [software]. Zenodo. https://doi.org/10.5281/zenodo.23762533.

Maas, J.M., Wittel, F.K., 2026c. Rheology data for Norway spruce [dataset]. Zenodo, v1.1. https://doi.org/10.5281/zenodo.23921788.

Massaro, F.M., Malo, K.A., 2019. Modelling the viscoelastic mechanosorptive behaviour of Norway spruce under long-term compression perpendicular to the grain. Holzforschung 73, 715–725.

Mohager, S., Toratti, T., 1992. Long term bending creep of wood in cyclic relative humidity. Wood Sci.Technol. 27, 49–59.

Müller, J., 2014. MATSuMoTo: The MATLAB surrogate model toolbox for computationally expensive black-box global optimization problems. arXiv:1404.4261 , 13arXiv:1404.4261.

Navi, P., Pittet, V., Plummer, C., 2002. Transient moisture effects on wood creep. Wood Sci. Technol. 36, 447–462.

Olsson, A.M., Salmén, L., 2001. Molecular mechanisms involved in creep phenomena of paper. J. Appl. Polym. Sci. 79, 1590–1595.

Olsson, A.M., Salmén, L., Eder, M., Burgert, I., 2007. Mechano-sorptive creep in wood fibres. Wood Sci. Technol. 41, 59–67.

Peng, H., Jiang, J., Lu, J., Cao, J., 2019. Orthotropic mechano-sorptive creep behavior of Chinese fir during the moisture adsorption process determined in tensile mode via dynamic mechanical analysis (DMA). Holzforschung 73, 229–239.

Peng, H., Jiang, J., Lu, J., Cao, J., 2020. Orthotropic hygro-mechanical behavior of Chinese fir during cyclical relative humidity variation. J. Wood Sci. 66, 19.

Perkowski, Z., Świrska-Perkowska, J., Gajda, M., 2017. Comparison of moisture diffusion coefficients for pine, oak and linden wood. J. Build. Phys. 41, 135–161.

Pyörälä, J., Piispanen, R., Valkonen, S., Lundqvist, S.O., 2022. Tracheid dimensions of Norway spruce in uneven-aged stands. Can. J. For. Res. 52, 346–356.

Ranta-Maunus, A., 1975. The viscoelasticity of wood at varying moisture content. Wood Sci. Technol. 9, 189–205.

Saft, S., Kaliske, M., 2011. Numerical simulation of the ductile failure of mechanically and moisture loaded wooden structures. Comput. Struct 89, 2460–2470.

Saifouni, O., Destrebecq, J.F., Froidevaux, J., Navi, P., 2016. Experimental study of the mechanosorptive behaviour of softwood in relaxation. Wood Sci. Technol. 50, 789–805.

Schmidt, J., Kaliske, M., 2006. Zur dreidimensionalen Materialmodellierung von Fichtenholz mittels eines Mehrflächen-Plastizitätsmodells. Holz Roh- Werkst. 64, 393–402.

Schniewind, A.P., 1966. Über den Einfluß von Feuchtigkeitsänderungen auf das Kriechen von Buchenholz quer zur Faser unter Berücksichtigung von Temperatur und Temperaturänderungen. Holz Roh. Werkst. 24, 87–98.

Siau, J.F., 1984. Transport Processes in Wood. Number 2 in Springer Series in Wood Science, Springer-Verlag Berlin Heidelberg.

Siau, J.F., Avramidis, S., 1996. The surface emission coefficient of wood. Wood Fiber Sci. 28, 178–185.

Simo, J., Hughes, T., 1998. Computational Inelasticity. Interdisciplinary Applied Mathematics. 1 ed., Springer, New York, NY.

Skaar, C., 1988. Wood-Water Relations. Springer Series in Wood Science, Springer, Berlin u.a.

Sonderegger, W., Vecellio, M., Zwicker, P., Niemz, P., 2011. Combined bound water and water vapour diffusion of Norway spruce and European beech in and between the principal anatomical directions. Holzforschung 65, 819–828.

Stevanic, J.S., Salmén, L., 2020. Molecular origin of mechano-sorptive creep in cellulosic fibres. Carbohydr. Polym. 230, 115615.

Stöcklein, J., Grajcarek, G., Konopka, D., Kaliske, M., 2024. Hygro-mechanical long-term behaviour of spruce, pine and lime wood: Parameter identification and model validation. Wood Sci. Technol. 58, 2007–2031.

Strömbro, J., Gudmundson, P., 2008. Mechano-sorptive creep under compressive loading – A micromechanical model. Int. J. Solids Struct. 45, 2420–2450.

Svensson, S., Toratti, T., 2002. Mechanical response of wood perpendicular to grain when subjected to changes of humidity. Wood Sci. Technol. 36, 145–156.

Toratti, T., 1992. Creep of Timber Beams in a Variable Environment. Number 31 in Teknillinen Korkeakoulu, Talonrakennustekniikan Julkaisusarja, Teknillinen korkeakoulu, talonrakennustekniikan laboratorio.

Toratti, T., Svensson, S., 2000. Mechano-sorptive experiments perpendicular to grain under tensile and compressive loads. Wood Sci. Technol. 34, 317–326.

Wilkins, A., Spencer, B.W., Jain, A., Gencturk, B., 2020. A method for smoothing multiple yield functions. Int. J. Numer. Methods Eng. 121, 434–449.

Wu, Q., Milota, M.R., 2007. Mechano-sorptive deformation of Douglas-fir specimens under tangential tensile stress during moisture adsorption. Wood Fiber Sci. 28, 128–132.

Yu, T., Khaloian, A., Van De Kuilen, J.W., 2022. An improved model for the time-dependent material response of wood under mechanical loading and varying humidity conditions. Eng. Struct. 259, 114116.

Zhou, Y., Fushitani, M., Kubo, T., 2000. Effect of stress level on bending creep behavior of wood during cyclic moisture changes. Wood Fiber Sci. 32, 20–28.

Zhou, Y., Fushitani, M., Kubo, T., Ozawa, M., 1999. Bending creep behavior of wood under cyclic moisture changes. J. Wood Sci. 45, 113–119.